Available online at www.sciencedirect.com

ScienceDirect

journal homepage: www.elsevier.com/locate/he

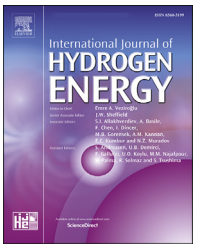

Thermal decomposition of titanium hydrides in electrochemically hydrogenated electron beam melting (EBM) and wrought Ti–6Al–4V alloys using *in situ* high-temperature X-Ray diffraction

Nissim U. Navi [a,**], *Brian A. Rosen* [b], *Eyal Sabatani* [a], *Jonathan Tenenbaum* [a], *Eitan Tiferet* [a,c], *Noam Eliaz* [b,*]

[a] *Nuclear Research Center Negev (NRCN), P.O. Box 9001, Beer Sheva, 84190, Israel*
[b] *Department of Materials Science and Engineering, Tel-Aviv University, Ramat Aviv, Tel Aviv, 6997801, Israel*
[c] *AM Center, Rotem Industries Ltd., Mishor Yamin, 86800, Israel*

HIGHLIGHTS

- Dehydrogenation of hydrogenated EBM and wrought Ti–6Al–4V alloys is compared.
- The kinetics and products of hydride decomposition are different in the two alloys.
- The differences result from different microstructures of the origin alloys.
- Decomposition of δ_a to δ_b is reported here for the first time.
- The EBM alloy may be more prone to hydrogen damage at elevated temperatures.

ARTICLE INFO

Article history:
Received 13 March 2021
Received in revised form
9 June 2021
Accepted 23 June 2021
Available online 15 July 2021

Keywords:
Additive manufacturing (AM)
Electron beam melting (EBM)
Ti–6Al–4V alloy
Titanium hydride
High-temperature X-ray diffraction (HTXRD)

ABSTRACT

Thermal decomposition of titanium hydrides in electrochemically hydrogenated electron beam melting (EBM) and wrought Ti–6Al–4V alloys containing 6 wt% β is compared. Differential scanning calorimetry (DSC) is used to identify phase transitions. High-temperature X-ray diffraction (HTXRD) is used to identify phases and determine their contents and crystallographic parameters. Both alloys are found to contain α_H (hcp) and β_H (bcc) solid solutions, as well as δ_a (fcc) and δ_b (fcc) hydrides after hydrogenation. δ_a is found to decompose between room temperature and 350 °C to α_H (in both alloys) plus either β_H and δ_b (wrought alloy) or δ_b only (EBM alloy). δ_b fully decomposes at either 450 °C (wrought alloy) or 600 °C (EBM alloy) to α_H plus H_2 desorption (which starts at 300 and 350 °C in the wrought and EBM alloys, respectively). In the case of the wrought alloy, β_H is also formed in this decomposition reaction due to faster diffusion of hydrogen. The non-continuous, finer needle-like morphology of the β-phase in the as-printed EBM alloy combined with its smaller lattice constants seem to inhibit hydrogen diffusion into the bulk alloy through the β-phase, thus triggering δ_a dissociation into δ_b (rather than to $\beta_H+\delta_b$) and δ_b decomposition into α_H (rather than to $\alpha_H + \beta_H$). Hydrogen incorporation in the α_H phase results in its expansion in the c direction in both alloys. HTXRD allows to conclude that both δ_a and δ_b hydrides decompose up to 600 °C. Hydrogen peaks measured at higher temperatures are due to hydrogen desorption from the hydride that is decomposed from the sample's bulk

* *Corresponding author.*
** *Corresponding author.*
E-mail addresses: NissimN@nrcn.gov.il (N.U. Navi), neliaz@tau.ac.il (N. Eliaz).
https://doi.org/10.1016/j.ijhydene.2021.06.166

and/or hydrogen desorption from β_H and/or α_H during heating. These findings indicate that the EBM Ti–6Al–4V alloy might be more prone to hydrogen damage at elevated temperatures than its wrought counterpart when both have a similar β-phase content.

Introduction

Ti–6Al–4V is a dual phase, α (hcp) + β (bcc) alloy with an attractive combination of properties. It is therefore the most commonly used Ti-based alloy in the aerospace, automotive and biomedical industries [1,2]. Given the unique, attractive properties of Ti-based alloys and the difficulty to manufacture complex parts from them by traditional processes such as casting and machining, it is not surprising that extensive efforts have been made in recent years to process them by additive manufacturing (AM), mainly for biomedical [3,4] and aircraft [5] applications.

A wide variety of microstructures of Ti–6Al–4V can be obtained (and, thus, diverse product's properties), which are broadly classified into three types: lamellar, equiaxed and bimodal. These microstructures can be tailored through control of the solution annealing temperature, cooling rate and final aging temperature [6]. Different AM technologies imply different microstructures and phase contents in AM'ed Ti–6Al–4V products, and consequently – different properties [7,8]. The microstructure of EBM Ti–6Al–4V typically consists of a primary α (hcp) phase and a small amount of β (bcc) phase [7,9]. Microstructural differences between wrought and EBM Ti–6Al–4V have also been discussed [10].

Ti–6Al–4V is susceptible to hydrogen damage [11]. Hydrogen might enter the alloy during processing, electroplating or other post-treatments, storage, corrosion, or cathodic protection [12,13]. A wide range is noticed in the reported values of hydrogen diffusivity [14,15] and solubility [16] in Ti–6Al–4V, which may be attributed to their dependence on the microstructure and β-phase content. Hydrogen in Ti–6Al–4V can diffuse preferentially through the β phase and react with the α phase along the α/β interphase boundaries to form brittle hydrides [12,17,18]. Three such hydrides have been observed at room temperature: δ (fcc), ε (fct with $c/a \leq 1$), and metastable γ (fct with $c/a > 1$) [19,20]. The presence of these hydrides in the alloy results in lattice expansion, strain, cracking, and eventually alloy degradation. Ti-based alloys processed by AM might be even more prone to hydrogen damage than their wrought counterparts due to a distinguished microstructure [18,21], porosity, residual thermal stresses, hydrogen absorption from the printed powder, etc. Therefore, it is important to study the interaction of hydrogen with AM'ed Ti–6Al–4V before this alloy can be used extensively as a construction material, particularly in critical applications.

Due to the wide interest in Ti alloys, extensive work has been conducted to explore the Ti–H phase diagram [22,23] and the phase boundaries of Ti–6Al–4V–xH [24–28]. The hydrogenation method and microstructural morphology were found to play a major role in the decomposition behavior of Ti–6Al–4V–xH. In most studies, hydrogenation was performed from a gaseous environment at high temperatures to enhance hydrogen diffusion from the surface into the bulk, in order to either achieve homogeneous composition and microstructure or study the high-temperature phase constitution [29]. High-temperature hydrogenation resulted in formation of phases such an orthorhombic martensite α'' [30], α_2 (Ti_3Al) [27], or α' [28,31]. Electrochemical hydrogenation, on the other hand, has been employed to less extent in the study of the phase boundaries of Ti–6Al–4V–xH because the hydrogenation is typically concentrated in vicinity of the metal surface, hence a concentration gradient is established between the surface and the bulk [12,32–34]. Decomposition differences between electrochemically charged and gaseous charged duplex-annealed Ti–6Al–4V alloy with 60 vol% equiaxed primary α and 40 vol% transformed β were demonstrated [35]. Electrochemically hydrogenated samples were claimed to contain α and β phases as well as a hydride phase and showed one major decomposition peak in temperature programmed desorption mass spectrometry (TPD-MS, also known as thermal desorption spectroscopy, TDS) between 562 and 580 °C. When the heating rate was increased, a shift was evident to higher temperatures. In contrast, hydrogenation from the gas phase resulted in the appearance of mostly a hydride phase and one major decomposition peak, albeit at lower temperatures, between 404 and 431 °C.

Hydrogen desorption from hydride-containing materials has been described as a series of five reaction partial steps: (1) hydride decomposition at the metal/hydride interface, (2) interstitial diffusion of hydrogen atoms from the hydride phase to the subsurface through a solid solution, (3) exit of hydrogen atoms through the surface, (4) chemisorption of hydrogen atoms on the surface, recombination of hydrogen atoms to hydrogen molecules, and physisorption of hydrogen molecules on the surface, and (5) desorption of molecular hydrogen to the gaseous environment [36]. Dehydrogenation investigations of Ti hydrides are widely conducted, mainly using δ-TiH_2 powders. Many studies have shown that the kinetics of TiH_2 decomposition can be controlled via control of the annealing atmosphere – vacuum [37–41], air [32,38,42], argon [33,42,43], nitrogen [42], and helium [38]. The dehydrogenation behavior has also been shown to be dependent on the original powder size [44] and the presence of an oxide layer on the surface of the hydride [45–47]. Bhosle et al. [38] showed that TiH_x phase containing less hydrogen than TiH_2 can be thermally stable at higher temperatures. The coexistence of α, β and δ in hydrogenated titanium annealed in argon was observed [45,48], and was attributed to hydrogen concentration gradient inside the TiH_2 decomposed particles [48]. TiH_2 was found to start releasing hydrogen at 375 °C under Ar flow and a heating rate of 10 °C/min [45]. The lattice parameter increased during heating until hydrogen release started, due

to thermal expansion, but then decreased [45]. The heating rate and mass transport conditions of Ar (namely, either flowing or stationary) changed the critical temperature and sequence of decomposition. Takasaki et al. [49] reported that δ in Ti precharged electrochemically is completely dissociated into α + β phases at ~327 °C, with an indication of hydride thermal instability at ~100 °C. Increasing the heating rate caused the dissociation temperature to increase. In another study, Blackburn et al. [16] studied absorption and desorption of hydrogen from Ti–6Al–4V powder pre-hydrogenated in a gaseous environment, and observed three desorption peaks when heated to 700 °C at a nominal heating rate of ~1 °C/s.

Studies of hydrogen in AM'ed Ti-based alloys are still rare, and have been focused on hydrogenation from the gaseous phase [14,50–54], although electrochemical hydrogenation behaves differently and in many cases resembles better the actual conditions [21]. In a recent study [54] it was reported that EBM Ti–6Al–4V hydrogenated electrochemically at a current density of −50 mA/cm^2 for 2 days contained cubic δ-TiH$_x$ and tetragonal γ-TiH hydrides, in addition to α and β phases. Navi et al. [21] have recently shown that Ti–6Al–4V EBM and wrought alloys, containing 6 wt% β in the non-charged condition, contained α/α$_H$ (hcp) and β$_H$ (bcc) solid solutions as well as δ$_a$ (fcc) and δ$_b$ (fcc) hydrides, which had not been reported before, following electrochemical hydrogenation at −25 mA/cm^2 for four days; the δ$_a$ and δ$_b$ hydrides were claimed to transform from the primary α phase. The hydrogen uptake was higher in the wrought alloy due to a lower lattice constant of the β phase and discontinuous arrangement of the β-phase particles along the short-transverse direction in the EBM alloy. The microstructure of the EBM alloy, with many α/β interphase boundaries, enhanced hydride formation, making the EBM alloy more susceptible to hydrogen-induced cracking along interphase boundaries. For both alloys, a single hydrogen desorption peak at ~620 °C was observed in the TPD spectra.

Hydrogen also has some positive effects on titanium and other metals, as well as on semiconductors. For example, it stabilizes the β phase [55], and is used as a temporary alloying element to improve the structural and thermomechanical properties of titanium [55,56]. Titanium hydride is commonly used for hydrogen (energy) storage applications, production of pure hydrogen for clean energy applications, bonding metals to non-metals, processing of nanocrystalline titanium and inexpensive titanium powders, as an agent for foaming aluminum and other metals, etc. [20,37,39,43–45]. These applications involve either full decomposition of the hydride or partial release of hydrogen from it during heat treatment in a controlled environment. Hence, the study of non-isothermal titanium hydride dissociation is of great technological importance, both for the improvement of existing applications and for the development of new ones [20,43,44]. Furthermore, hydrogen desorption processes may be different in AM'ed alloys compared to their wrought counterparts due to differing microstructures, trap density, and binding energy. Therefore, here we extend our previous studies [18,21] and investigate the thermal stability and decomposition of the δ$_a$ and δ$_b$ hydrides in EBM and wrought Ti–6Al–4V alloys that are hydrogenated electrochemically for four days. To this aim, we utilize high-temperature X-ray diffraction (HTXRD) and differential scanning calorimetry (DSC).

Materials and methods

Sample preparation and electrochemical hydrogenation

EBM Ti–6Al–4V, Grade 5, was processed in an Arcam Q20 Plus machine at the AM Center of Rotem Industries Ltd. (Mishor Yamin, Israel). Wrought Ti–6Al–4V, Grade 23 (ASTM F136) was produced by Dynamet, Inc. (Washington, PA). Both alloys were found to contain ~6 wt% β phase [21], therefore any possible effect of the content of this phase on different behaviors of the two alloys can be excluded. Samples with nominal dimensions of 18 × 18 × 0.3 mm^3 were cut by electric discharge machining (EDM), mechanically ground and polished on both sides down to 1 μm abrasive. Surface activation was done by rinsing the polished samples for 15 s in a solution of 2.5 N HNO_3 with 20 g/L NaF, followed by rinsing in distilled water. Electrochemical hydrogenation was carried out galvanostatically (j = −25 mA/cm^2) at room temperature (RT) for four days. H_3PO_4:glycerin (1:2 vol) [21,57,58] was the electrolyte; a fresh solution was prepared for each experiment. The electrolyte was purged with Ar for 30 min before charging started. Purging continued above the electrolyte during charging to prevent oxygen absorption. The Ti–6Al–4V sample was the cathode, while a cylindrical $Pd_{90}Pt_{10}$ (wt.%) sheet surrounding it was the anode.

Chemical and microstructural characterization

Chemical composition was determined by glow discharge optical emission spectrometry (GDOES), oxygen/nitrogen/hydrogen analyzer, and energy-dispersive X-ray spectroscopy (EDS) [21]. Density was determined by the Archimedes method [21]. Microstructural analysis was performed by metallography, scanning and transmission electron microscopy, and XRD [21]. Hydrogen mapping and desorption analyses were carried out by means of time-of-flight secondary ion mass spectrometry (ToF-SIMS) [21,59] and temperature programmed desorption mass spectrometry (TPD-MS) [21,33,47,57,60].

DSC analysis

The combination of DSC and TPD allows a thorough study of the thermodynamics and kinetics of titanium hydrides and their dissociation, with possibility to relate peaks in the TPD spectrum to phase transformations [20]. Here, thermal analysis was performed using a DSC 404 F3 Pegasus® NETZSCH differential scanning calorimeter. Small pieces of non-hydrogenated and four-day hydrogenated Ti–6Al–4V samples, weighing 12–15 mg, were cut from the hydrogenated samples to fit into the small alumina crucibles. A sample made of commercially pure Ti (CP–Ti, Grade 2, ASTM F67–00, max 0.25 wt% O, 5 mm thick plate, supplied by Barmil Ltd.), weighing ~7 mg, was used to evaluate the DSC baseline sensitivity. The scans were run from RT to ~1000 °C at a heating rate of 15 °C/min (similar to the TPD conditions reported in Ref. [21]) in an ultrahigh purity Ar atmosphere, using a heat-flux DSC sensor. There was no visual evidence of chemical reaction between the alumina crucibles and the Ti–6Al–4V samples after any of the DSC runs.

HTXRD analysis

HTXRD is a powerful technique for verification of the sequence of phase transformations [20,37,39], although some delay in the dehydrogenation, compared to DSC and TPD, might appear in HTXRD due to higher levels of oxygen in the test chamber [20]. Here, HTXRD measurements were performed in a D8 Advance diffractometer (Bruker AXS, Madison, WI, USA) with a Bragg-Brentano geometry and a Cu-Kα radiation source. Samples were placed on a Macor sample stage in an Anton Paar XRK-900 high-temperature reaction chamber. The contribution of the thermal expansion of the stage was first measured by calibrating the stage height as a function of temperature with an alignment slit. The temperature of the sample was controlled with an Anton Paar TCU 750 controller by mounting a K-type thermocouple in the sample holder adjacent to the sample, using a heating rate of 10 °C/min. Diffractograms were acquired between RT and 600 °C. A linear position sensitive device (PSD) detector (LYNXEYE XE-T) was used, with an opening of 2.94°. The diffraction pattern was recorded from $2\theta = 10°$ to $2\theta = 120°$ using a coupled theta/two-theta scan type. Data points were acquired at increments of 0.02° and an acquisition time of 0.5 s. The lattice parameters were fitted by Rietveld refinement, using TOPAS software ver. 5 (Bruker AXS, Madison, WI, USA). The refined parameters included the lattice parameters, relative phase content, sample displacement, zero error, domain size, and the preferred orientation of the sample. Peak position and the effect of instrumental broadening and asymmetry were calibrated using SRM Si 640f and LaB_6 660c standard reference materials, respectively.

Results and discussion

Herein, the thermal stability and decomposition characteristics of δ_a and δ_b hydrides in EBM and wrought Ti–6Al–4V alloys are compared. The microstructure of both non-hydrogenated and four-day hydrogenated alloys, as well as hydrogen release from four-day hydrogenated alloys, were described in detail in Ref. [21]. Since both non-hydrogenated alloys contained ~6 wt% β and had similar density and microstrain [21], any difference in the hydride decomposition behavior between the EBM and wrought Ti–6Al–4V alloys should be attributed to their different microstructures.

DSC thermograms of non-hydrogenated wrought and EBM Ti–6Al–4V alloys as well as of CP-Ti are shown in Fig. 1a. The α → β transformation can be clearly seen in the CP-Ti thermograms at ca. 900 °C, confirming the sensitivity of the measurement setup. A similar transformation is not apparent in both non-hydrogenated alloys. DSC thermograms of both hydrogenated alloys are shown in Fig. 1b. Although DSC data was collected up to ~1000 °C, data analysis is discussed herein only up to ~800 °C, where the hydrides decompose. In the hydrogenated alloys, two endothermic transitions are observed. The first transition has temperature maxima at 296 °C and 280 °C for the wrought and EBM alloys, respectively. The wrought alloy shows a higher intensity, broader peak compared to the EBM alloy, presumably due to higher hydrogen uptake in the wrought alloy than in the EBM alloy

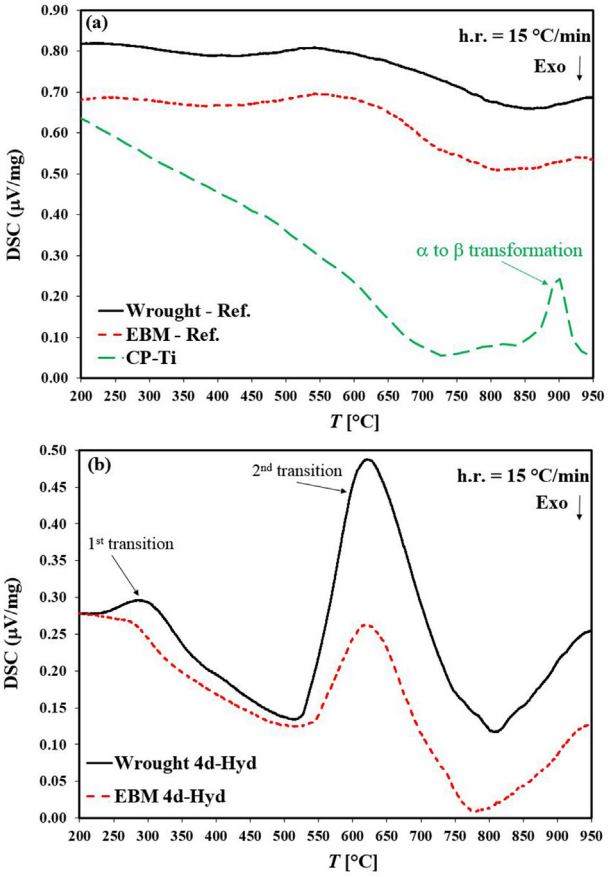

Fig. 1 – DSC thermograms of (a) non-hydrogenated wrought and EBM Ti–6Al–4V alloys and CP-Ti, and (b) hydrogenated wrought and EBM alloys. The y-axes values are after an arbitrary shift.

[21]. This phase transition cannot be associated with hydrogen desorption because no hydrogen desorption was observed around this temperature in the TPD spectra [21]. Therefore, it is suggested that hydrogen originating from hydride dissociation was dissolved in the bulk alloy, as reported in Refs. [49,54].

The second endothermic transition starts at 520 °C and 527 °C and ends at 808 °C and 784 °C for the wrought and EBM alloys, respectively, with a maximum at ~625 °C for both alloys. These broad, continuous peaks appear at higher temperatures compared to their respective peaks in the TPD spectra, where hydrogen desorption starts at ~400 °C and the maximum is at ~620 °C [21]. Since both DSC and TPD were performed with flowing gas (Ar and He, respectively) using similar heating rates (10–20 and 15 °C/min, respectively), it can be concluded that the difference in reaction temperatures does not originate from differences in the heating rates and/or experimental environment (say, flowing gas vs. vacuum). This suggests that hydrogen release from the alloy between 400 and 520 °C is due to reduction in hydride stoichiometry that is not accompanied by phase transformation (release above 520 °C will be discussed below). The higher transition range of the wrought alloy is attributed to larger hydrogen concentration in this alloy compared to the EBM alloy [21].

XRD patterns at temperatures between RT and 600 °C are shown in Fig. 2 for both hydrogenated wrought and EBM Ti–6Al–4V alloys. The XRD patterns of both non-hydrogenated alloys are shown as well. It is evident that the XRD peaks are relatively broad. Peak broadening in titanium alloys may result from microscopic internal stresses [61], lattice distortion [62], wide phase compositional range [61], crystallite size reduction [63], and amorphization [63,64]. Although the contribution of each possible effect cannot be deconvolved from our data, a Rietveld fit showed a nano-metric domain size (<200 nm) for all phases: 62–179 nm and 37–150 nm (varied with temperature) α and β domain sizes, respectively, in the non-hydrogenated wrought alloy; 67–76 nm and 10–18 nm α and β domain sizes, respectively, in the non-hydrogenated EBM alloy; 16–32 nm, 10–18 nm, 11–14 nm, and 10–24 nm domain sizes of α/α_H, β_H, δ_a, and δ_b, respectively, in the hydrogenated wrought alloy; 26–34 nm, 10–24 nm, 10–17 nm, and 10–30 nm domain sizes of α/α_H, β_H, δ_a, and δ_b, respectively, in the hydrogenated EBM alloy. Hence, nano-domains seem to play a role in peak broadening. At RT, both alloys contain α/α_H (space group $P6_3mmc$ [48]) and β_H (space group $Im\bar{3}m$ [48]) solid solutions, as well as δ_a and δ_b hydrides (space group $Fm\bar{3}m$), similar to our observations in Ref. [21]. The δ_a hydride in both alloys is stable up to 350 °C, while the δ_b hydride is stable up to ~450 °C and 600 °C in the wrought and EBM alloys, respectively. Reflections related to the α/α_H phase were observed above $2\theta = 50°$, but are not included in Fig. 2 because they are comparatively minor.

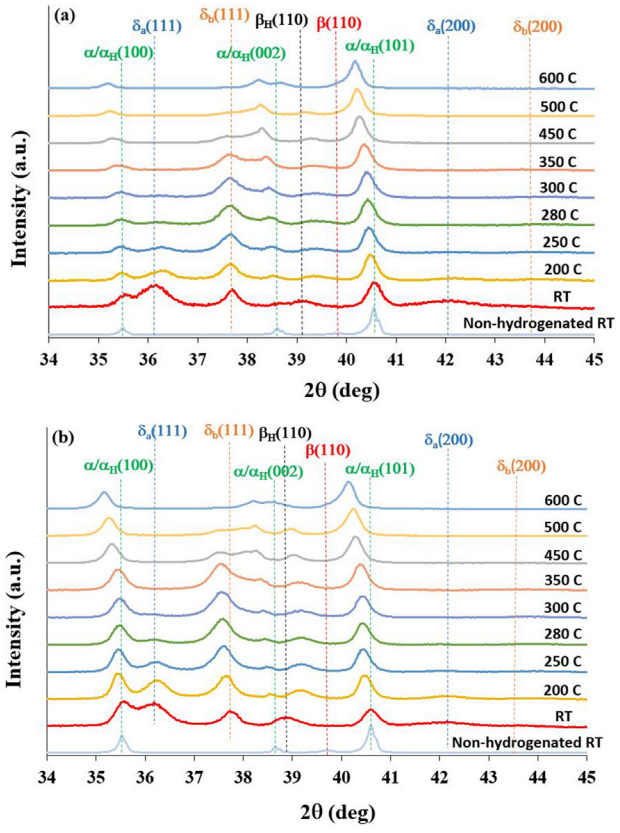

Fig. 2 – XRD patterns at different temperatures from both electrochemically hydrogenated Ti–6Al–4V alloys. (a) EBM alloy, (b) wrought alloy.

Analysis of the phase contents in both non-hydrogenated and four-day hydrogenated Ti–6Al–4V alloys is provided in Fig. 3 within the temperature range of RT to 500 °C. Although HTXRD data was collected up to 600 °C, Rietveld refinement is reported herein only up to 500 °C, above which unidentified phases (probably oxides) and/or peak distortions made proper fitting infeasible.

In both non-hydrogenated alloys, the α and β contents are constant within the entire temperature range. In the case of the hydrogenated alloys, however, the α/α_H phase content is significantly lower at RT compared to that of α in the non-hydrogenated alloys. This is due to the tendency of δ_a and δ_b to be formed from the primary α phase, in agreement with [21]. The α/α_H phase content in the wrought alloy increases significantly and gradually with temperature up to 450 °C (and then decreases), while that in the EBM alloy increases up to 500 °C (reaching its original relative content in the non-hydrogenated state). At RT, the β/β_H phase content in both hydrogenated alloys (Fig. 3b) is similar to that of β in the non-hydrogenated alloys, in agreement with [21]. The β_H content in the wrought alloy is constant up to 200 °C, above which it gradually increases. In contrast, the β_H content in the EBM alloy is almost unchanged up to 500 °C, but then it drops to ~0%. The differences in the β_H behavior in both alloys are attributed to microstructural effects. The wrought alloy is characterized by large β grains forming a continuous network [21]. Therefore, while heating the alloy, hydrogen diffuses from the bulk through the continuous β_H phase grains, stabilizing the β_H phase [56] and increasing its amount. Conversely, the discontinuous small β grains of the EBM alloy prevent hydrogen diffusion from the bulk, thus the β_H content is almost unchanged.

From Fig. 3c it is evident that the content of δ_a is similar in both hydrogenated alloys at RT. The δ_a content decreases gradually due to its decomposition into mainly the α_H phase, until full decomposition at 350 °C (in both alloys). In the wrought alloy, the minor β_H phase and δ_b hydride are also formed, whereas in the EBM alloy δ_b hydride is the only minor product of the δ_a decomposition. The δ_a decomposition products in the wrought alloy in this study are partially consistent with the results in Ref. [49], where δ in electrochemically hydrogenated Ti was completely dissociated into α + β phases at ~327 °C. Similar observations to Ref. [49] were reported for electrochemically hydrogenated EBM Ti–6Al–4V [54]. Thus, the formation of δ_b as a decomposition product of δ_a is reported here for the first time. Nevertheless, the decomposition of the EBM δ_a phase into the sole minor δ_b hydride, and not into both minor β_H phase and δ_b hydride as in the wrought alloy, can be attributed to the discontinuous (and, thus, less available), finer needle-like β-phase particles and to the smaller lattice constants (to be discussed below) in the EBM alloy. The relatively higher amount of δ_a in the wrought alloy compared to the EBM alloy, during its decomposition between 200 and 280 °C, may result from slower decomposition kinetics of δ_a in the wrought alloy. It may also indicate that a further generation of δ_a hydride occurs due to continuous hydrogen diffusion from the bulk, which is more favorable in the wrought alloy compared to the EBM one, as suggested above.

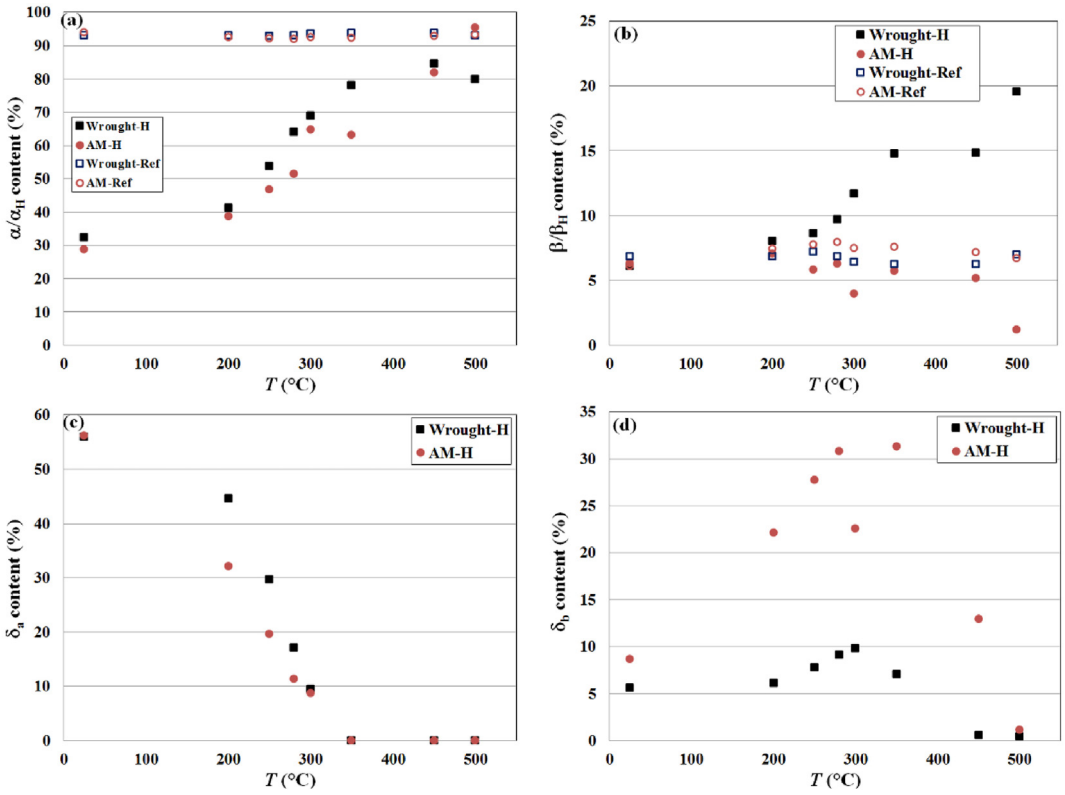

Fig. 3 – Phase contents in both non-hydrogenated and electrochemically hydrogenated Ti–6Al–4V alloys versus temperature. (a) α/α_H phase, (b) β/β_H phase, (c) δ_a hydride, (d) δ_b hydride.

The content of the δ_b hydride is similar in both hydrogenated alloys at RT (Fig. 3d). The content of the δ_b in the wrought alloy slightly increases during heating up to 300 °C, but then drops until full decomposition at 450 °C. In contrast, its content in the EBM alloy increases significantly with temperature up to 350 °C, and then drops until nearly full decomposition only at 600 °C. A residual δ_b peak is still present at 600 °C; however, its amount could not be accurately quantified with Rietveld analysis, as explained above.

The apparent differences in the δ_b decomposition behavior for the two alloys may be attributed to the higher δ_b content in the EBM alloy and/or to slower decomposition kinetics in the EBM alloy. However, the concurrent decreasing content of the δ_a hydride and the increasing content of the δ_b hydride in the EBM alloy when heating may be an indication of a localized δ_a-to-δ_b hydride phase transformation, which becomes favorable due to hindered hydrogen diffusion in the EBM alloy, as suggested above. This hindered diffusion may also be the reason for the higher temperature needed to complete the decomposition of the δ_b hydride phase.

The final decomposition of the δ_b hydride above 350 °C into α_H (major) + β_H (minor) in the wrought alloy and into α_H phase in the EBM alloy are consistent with reports on the coexistence of α, β and δ at high temperatures in an Ar environment [45,48]. The decomposition of δ_b hydride in the EBM alloy into α_H, rather than to $\alpha_H + \beta_H$, again reflects the hindered diffusion of hydrogen in the α-phase and the discontinuity of the β phase in the EBM alloy.

Analysis of the change in lattice parameters with temperature is shown in Fig. 4 for both non-hydrogenated and electrochemically hydrogenated Ti–6Al–4V alloys. The differences between the maximal and minimal lattice parameter values (i.e. expansion in percentage for each phase for the whole temperature range) is presented in Fig. 4f. For the non-hydrogenated alloys, it is evident from Fig. 4 that the lattice parameters *a* (Fig. 4a) and *c* (Fig. 4b) of the α(hcp) phase are similar in the wrought and in the EBM alloys; they gradually expand with temperature due to thermal expansion. The lattice parameter *a* of the cubic β phase (Fig. 4c) in the non-hydrogenated wrought alloy at RT is larger than in the non-hydrogenated EBM alloy, and in agreement with the values reported in Ref. [21]. The expansion rates of the lattice parameters *a* and *c* of the α phases and of the lattice parameter *a* of the cubic β phase in the non-hydrogenated alloys are similar to those estimated in Ref. [65].

For the hydrogenated alloys, it is evident from Fig. 4 that the lattice parameter *a* of the α/α_H phase in both alloys expands gradually with temperature (Fig. 4a). The lattice parameter *c* of the α/α_H phase in both alloys expands significantly in comparison to the equivalent values in the non-hydrogenated alloys (Fig. 4b), with larger *c* values in the wrought alloy and a maximum at 450 and 500 °C in the wrought and EBM alloys, respectively. The increase of the *c* value in the hydrogenated α/α_H phase compared to the non-hydrogenated phase indicates hydrogen absorption in the original α phase during heating, forming α_H phase with

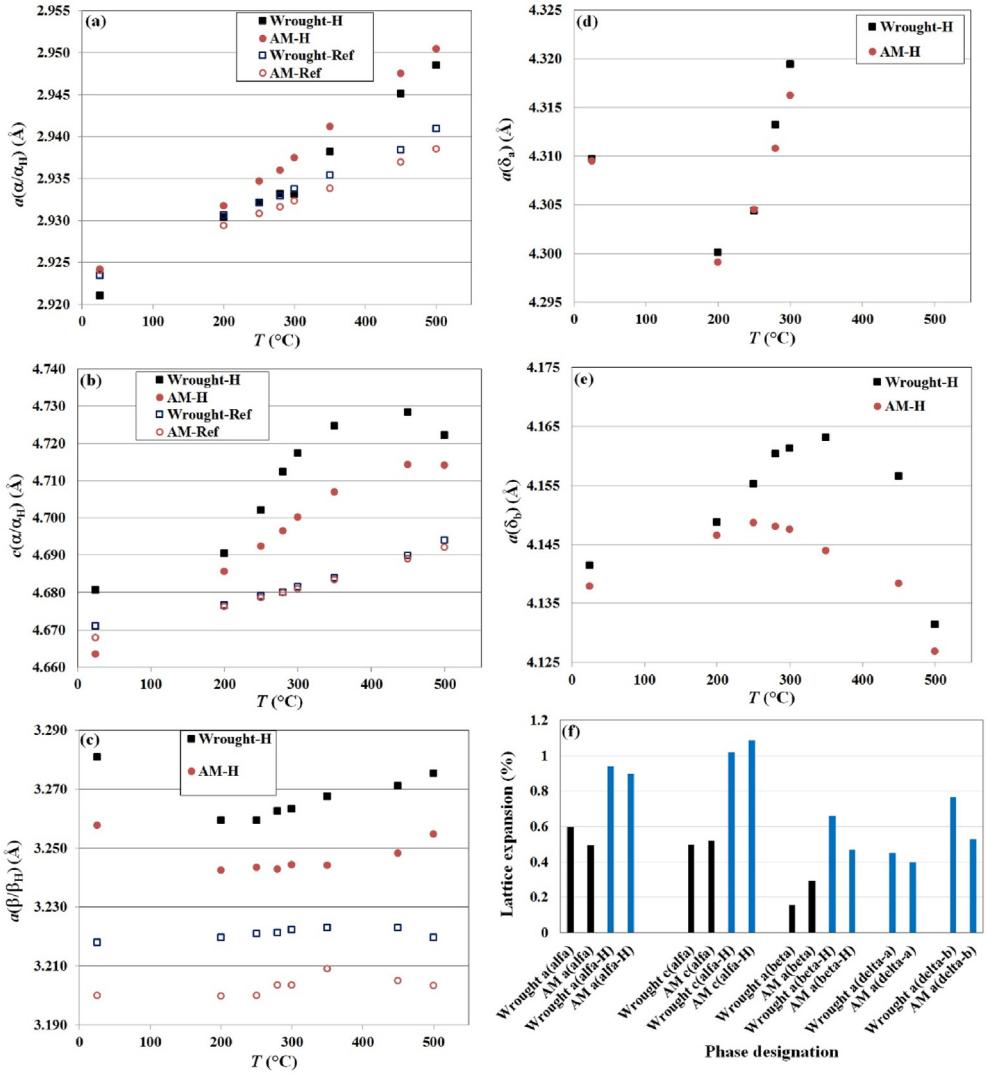

Fig. 4 – Changes in lattice parameters in both non-hydrogenated and electrochemically hydrogenated Ti–6Al–4V alloys during heating from RT. (a) *a* of the α/α_H phase, (b) *c* of the α/α_H phase, (c) *a* of the β/β_H phase, (d) *a* of the δ_a hydride, (e) *a* of the δ_b hydride, and (f) percent expansion of the lattice parameters of all phases, between start and end temperatures.

preferred expansion in the *c* direction (hence, at temperatures higher than RT, the hcp phase is α_H). The lattice parameter *c* of the α_H phase in the wrought alloy decreases at 500 °C, in agreement with the decrease in the α_H phase content in the wrought alloy shown in Fig. 3a. This suggests hydrogen release from the α_H phase.

At RT, the lattice parameter *a* values of the β_H phase in the hydrogenated alloys are larger than the corresponding values in the non-hydrogenated β phase (Fig. 4c), indicating the formation of β_H solid solution. The *a* values are larger for the wrought alloy compared to the EBM alloy, in agreement with what reported in Ref. [21] for RT. The larger *a* value of the β_H phase in the wrought alloy compared to the EBM alloy is maintained over the whole temperature range. In both hydrogenated alloys, the *a* value decreases during heating from RT to 200 °C, possibly suggesting a compositional change in β_H within this temperature range.

The lattice parameter *a* of the δ_a hydride is similar in both alloys and contracts when the alloy is heated from RT to 200 °C (Fig. 4d), possibly indicating a compositional change in δ_a during heating. Above 200 °C, a gradual increase in *a* is observed up to full decomposition at 350 °C. The gradual increase in the lattice parameter of δ_a above 200 °C may be associated to thermal expansion being more significant than compositional changes, if any, in this hydride, until full decomposition. The lattice parameter *a* of the δ_b hydride is similar in both alloys in the temperature range from RT to 200 °C (Fig. 4e). The lattice parameter *a* is smaller for δ_b hydride than for the δ_a hydride. This indicates a different composition of the hydride, presumably lower hydrogen stoichiometry, as reported in Ref. [44]. This assumption is in agreement with the tendency for higher temperature stability of the TiH_x hydride with lower hydrogen content reported in Ref. [44]. Above 200 °C, the lattice parameter of δ_b increases significantly in the wrought alloy up to 350 °C, and then decreases until full decomposition at 500 °C. The maximum at 350 °C is similar to the maximum at 375 ± 5 °C observed elsewhere [48] for the δ-phase in TiH_2 powder. The

larger expansion of the lattice parameter *a* with temperature for δ_b in the wrought alloy compared to the EBM alloy suggests a larger coefficient of thermal expansion. The maxima in lattice expansion values shown in Fig. 4f indicate higher expansion of *c* in the α_H phase.

To summarize, hydrogenation of both wrought and EBM Ti–6Al–4V alloys containing 6 wt% β results in the formation of δ_a and δ_b hydrides, following the reaction:

$$\alpha(\text{hcp}) \rightarrow \delta_a(\text{fcc}) + \delta_b(\text{fcc}) \quad (1)$$

These hydrides were recently reported by us for the first time [21]. With regard to δ_a, in both hydrogenated alloys δ_a fully decomposes at 350 °C, and its lattice parameter *a* is minimal at 200 °C, but the decomposition reactions differ:

$$\delta_a \rightarrow \alpha_H + \delta_H + \delta_b \text{ Wrought alloy} \quad (2)$$

$$\delta_a \rightarrow \alpha_H + \delta_b \text{ EBM alloy} \quad (3)$$

In both hydrogenated alloys, δ_b is first formed up to either 350 °C or 300 °C in the EBM and wrought alloys, respectively. Then, it starts dissociating until it is nearly fully decomposed at 600 °C, as suggested from the trends in the derived content and lattice parameters. The continuous network of β grains in the wrought alloy facilitates hydrogen diffusion and provides a route for long-distance migration of hydrogen from a localized δa hydride, forming the β_H phase. In contrast, in the EBM alloy the discontinuous small β grains deter hydrogen diffusion, and consequently – the formation of β_H phase; instead, it promotes a localized δ_a-to-δ_b hydride transformation.

The high-temperature decomposition reactions of δ_b are also different in the two alloys. The following schemes for δ_b decomposition reactions for the two alloys are suggested:

$$\delta_b \rightarrow \alpha_H + \beta_H + \uparrow H_2 \text{ (starting ~300 °C) Wrought alloy} \quad (4)$$

$$\delta_b \rightarrow \alpha_H + \uparrow H_2 \text{ (starting ~350 °C) EBM alloy} \quad (5)$$

At either 280 °C (EBM alloy, DSC data) or 296 °C (wrought alloy, DSC data), significant hydrogen release from the hydrides into the solid solutions in the bulk alloy is observed.

There is an apparent discrepancy between the HTXRD results, which indicate hydride full decomposition at 600 °C, and the TPD and DSC results that reveal hydrogen peaks at 620 and 625 °C, respectively. However, based on the HTXRD results we can distinguish between hydrides decomposition (up to 600 °C) and other hydrogen release effects. Due to the maximum hydrogen desorption peaks that were observed in TPD at ~620 °C [21] we may conclude that δ_b hydride contributes more to the aforementioned hydrogen release. The hydrogen desorption shown in TPD at temperatures higher than 600 °C is not attributed to a difference in kinetics due the different environments in the DSC and XRD chambers [42,45] (as was explained in the experimental section); instead, it is attributed to hydrogen desorption from the hydride decomposing in the sample's bulk and/or hydrogen desorption from β_H and α_H during heating above 600 °C.

The sequences of decomposition reactions shown above are somewhat different than those suggested before [20,39,41,45,48] for decomposition of titanium hydride, $\delta(TiH_2)$, in pure titanium hydride powders. On the other hand, there are some consistencies between the sequences reported elsewhere for titanium hydride in wrought CP-Ti [49], or δ-TiH_x in electrochemically hydrogenated EBM Ti–6Al–4V [54], and those observed in the present work for decomposition of the δ_a hydride in wrought Ti–6Al–4V. The complete decomposition of δ_b at 600 °C is also consistent with the complete decomposition of δ-hydride in titanium hydride powder reported elsewhere [37]. Discrepancies between the findings in different reports may be related to different behaviors in gaseous vs. electrochemically charged materials, sheets vs. powder samples, hydrides in CP-Ti vs. Ti–6Al–4V, hydrides in EBM Ti–6Al–4V vs. wrought Ti–6Al–4V, different heating rates, different test environments, isothermal vs. non-isothermal dehydrogenation conditions, oxidation and contamination in the test chamber, etc.

Conclusions

The microstructural effect on hydrides formation and thermal decomposition in four-day electrochemically hydrogenated electron beam melted (EBM) and wrought Ti–6Al–4V alloys (both with 6 wt% β content) was studied. In both alloys, hydrogen incorporation into the α_H phase resulted in preferential expansion in the *c*-direction of the hcp structure. HTXRD measurements showed that the kinetics and the products of thermal hydride decomposition are different in the two alloys. The dissociation of δ_a hydride was slower in the wrought alloy than in the EBM alloy due to slower kinetics and/or faster hydrogen diffusion in the wrought alloy than in the EBM alloy. It is suggested that the non-continuous, finer needle-like β-phase particles with smaller lattice constants in the non-hydrogenated EBM alloy inhibit hydrogen diffusion, thus imposing δ_a decomposition into δ_b instead of into $\beta_H + \delta_b$, and δ_b decomposition into α_H instead of into $\alpha_H + \beta_H$.

Declaration of competing interest

The authors declare that they have no known competing financial interests or personal relationships that could have appeared to influence the work reported in this paper.

Acknowledgements

This work was supported by grant No. 322/20 from the Pazi Foundation of the Israel Atomic Energy Commission and the Israeli Council of Higher Education. The authors thank Michael Chonin and Yaron I. Ganor for EBM of Ti–6Al–4V, Dr. Eli Brosh and Michaele Amos for DSC measurements, Eliran Hamo for XRD measurements, Prof. Giora Kimmel for

fruitful discussions on XRD, David Hai David for sample preparation, and David Svetlizky from TAU for general technical assistance.

REFERENCES

[1] Veiga C, Davim JP, Loureiro AJR. Properties and applications of titanium alloys: a brief review. Rev Adv Mater Sci 2012;32:133–48.

[2] Eliaz N. Corrosion of metallic biomaterials: a Review. Materials 2019;12. article 407.

[3] Hong S-B, Eliaz N, Sachs EM, Allen SM, Latanision RM. Corrosion behavior of advanced Ti-based alloys made by three-dimensional printing (3DP™) for biomedical applications. Corrosion Sci 2001;43:1781–91.

[4] Hong S-B, Eliaz N, Leisk GG, Sachs EM, Latanision RM, Allen SM. A new Ti-5Ag alloy for customized prostheses by three-dimensional printing (3DP™). J Dent Res 2001;80:860–3.

[5] Eliaz N, Fuks N, Geva D, Oren S, Shriki N, Vaknin D, Fishman D, Levi O. Comparative quality control of titanium alloy Ti–6Al–4V, 17–4 PH stainless steel, and aluminum alloy 4047 either manufactured or repaired by Laser Engineered Net Shaping (LENS®). Materials 2020;13. article 4171.

[6] Rack HJ, Qazi JI. Titanium alloys for biomedical applications. Mater Sci Eng C 2006;26:1269–77.

[7] Rafi HK, Karthik NV, Gong H, Starr TL, Stucker BE. Microstructures and mechanical properties of Ti6Al4V parts fabricated by selective laser melting and electron beam melting. J Mater Eng Perform 2013;22:3872–83.

[8] Herzog D, Seyda V, Wycisk E, Emmelmann C. Additive manufacturing of metals. Acta Mater 2016;117:371–92.

[9] Al-Bermani SS, Blackmore ML, Zhang W, Todd I. The origin of microstructural diversity, texture, and mechanical properties in electron beam melted Ti-6Al-4V. Metall Mater Trans A 2010;41:3422–34.

[10] Murr LE, Esquivel EV, Quinones SA, Gaytan SM, Lopez MI, Martinez EY, Medina F, Hernandez DH, Martinez E, Martinez JL, Stafford SW, Brown DK, Hoppe T, Meyers W, Lindhe U, Wicker RB. Microstructures and mechanical properties of electron beam-rapid manufactured Ti–6Al–4V biomedical prototypes compared to wrought Ti–6Al–4V. Mater Char 2009;60:96–105.

[11] Madina V, Azkarate I. Compatibility of materials with hydrogen. Particular case: hydrogen embrittlement of titanium alloys. Int J Hydrogen Energy 2009;34:5976–80.

[12] Eliaz N, Gileadi E. Physical electrochemistry: fundamentals, techniques, and applications. 2nd ed. Weinheim, Germany: Wiley-VCH; 2019. Ch. 17.

[13] Kudiiarov VN, Syrtanov MS, Bordulev YuS, Babikhina MN, Lider AM, Gubin VE, Murashkina TL. The hydrogen sorption and desorption behavior in spherical powder of pure titanium used for additive manufacturing. Int J Hydrogen Energy 2017;42:15283–9.

[14] Pushilina N, Syrtanov M, Kashkarov E, Murashkina T, Kudiiarov V, Laptev R, Lider A, Koptyug A. Influence of manufacturing parameters on microstructure and hydrogen sorption behavior of electron beam melted titanium Ti-6Al-4V alloy. Materials 2018;11. article 763.

[15] Hirohata Y, Aihara Y, Hino T, Miki N, Nakagawa S. Evaluation of hydrogen sorption and desorption for Ti-6A1-4V alloy as a vacuum vessel material. 1997. In: Varandas C, Serra F, editors. Proc. 19th symp. Fusion technology, vol. 1. New York, NY, USA: Elsevier; 1996. p. 363–6.

[16] Blackburn JL, Parilla PA, Gennett T, Hurst KE, Dillon AC, Heben MJ. Measurement of the reversible hydrogen storage capacity of milligram Ti–6Al–4V alloy samples with temperature programmed desorption and volumetric techniques. J Alloys Compd 2008;454:483–90.

[17] Kim J, Tasan CC. Microstructural and micro-mechanical characterization during hydrogen charging: an in situ scanning electron microscopy study. Int J Hydrogen Energy 2019;44:6333–43.

[18] Brosh E, Navi NU, Rosen BA, Eliaz N. Microvoids in electrochemically hydrogenated titanium-based alloys. Int J Hydrogen Energy 2021. https://doi.org/10.1016/j.ijhydene.2021.05.187.

[19] Tsai MM, Howe JM. Lengthening kinetics of (0110)γ-TiH precipitates in α-Ti in the temperature range of 25 °C to 80 °C. Metall Mater Trans A 1995;26:2219–26.

[20] Ma M, Liang L, Wang L, Wang Y, Cheng Y, Tang B, Xiang W, Tan X. Phase transformations of titanium hydride in thermal desorption process with different heating rates. Int J Hydrogen Energy 2015;40:8926–34.

[21] Navi NU, Tenenbaum J, Sabatani E, Kimmel G, Ben David R, Rosen BA, Barkay Z, Ezersky V, Tiferet E, Ganor YI, Eliaz N. Hydrogen effects on electrochemically charged additive manufactured by electron beam melting (EBM) and wrought Ti–6Al–4V alloys. Int J Hydrogen Energy 2020;45:25523–40.

[22] Okamoto H. H–Ti (hydrogen-titanium). J Phase Equilibria Diffus 2011;32:174–5.

[23] Wang K, Kong X, Du J, Li C, Li Z, Wu Z. Thermodynamic description of the Ti–H system. Calphad 2010;34:317–23.

[24] Kerr WR, Smith PR, Rosenblum ME, Gurney FJ, Mahajan YR, Bidwell LR. In: Kimura H, Izumi O, editors. Hydrogen as an alloying element in titanium (hydrovac), in Titanium 80: Science and Technology, vol. 4. Warrendale, PA: TMS; 1980. p. 2477–86.

[25] Qazi JI, Senkov ON, Rahim J, Genc A, Froes FH. Phase transformations in Ti–6Al–4V–xH alloys. Metall Mater Trans A 2001;32:2453–63.

[26] Zhu T, Li M. Effect of 0.770 wt%H addition on the microstructure of Ti–6Al–4V alloy and mechanism of δ hydride formation. J Alloys Compd 2009;481:480–5.

[27] Sun P, Fang ZZ, Koopman M, Paramore J, Ravi Chandran KS, Ren Y, Lu J. An experimental study of the (Ti–6Al–4V)–xH phase diagram using in situ synchrotron XRD and TGA/DSC techniques. Acta Mater 2015;84:29–41.

[28] Zong Y, Huang S, Guo B, Shan D. In situ study of phase transformations in Ti–6Al–4V–xH alloys. Trans Nonferrous Metals Soc China 2015;25:2901–11.

[29] Singh RN, Kishore R, Mukherjee S, Roychowdhury S, Srivastava D, Sinha TK, Dem PK, Bamerjee S, Kameswaran R, Sheelvantra SS, Gopalan B. Hydrogen charging, hydrogen content analysis and metallographic examination of hydride in zirconium alloys. Report no. BARC/2003/E/034 Bhabha Atomic Research Centre 2003. Mumbai, India.

[30] Luo L, Su Y, Guo J, Fu H. Formation of titanium hydride in Ti–6Al–4V alloy. J Alloys Compd 2006;425:140–4.

[31] Liu HJ, Zhou L, Liu P, Liu QW. Microstructural evolution and hydride precipitation mechanism in hydrogenated Ti–6Al–4V alloy. Int J Hydrogen Energy 2009;34:9596–602.

[32] Millenbach P, Givon M. The electrochemical formation of titanium hydride. J Less Common Met 1982;87:179–84.

[33] Verbeken K. Analysing hydrogen in metals: bulk thermal desorption (TDS) methods. 2. In: Gangloff RP, Somerday BP, editors. Gaseous hydrogen embrittlement of materials in energy technologies, vol. 2. Cambridge, UK: Woodhead Publishing Limited; 2012. p. 27–55.

[34] Iyer RN, Pickering HW. Mechanism and kinetics of electrochemical hydrogen entry and degradation of metallic systems. Annu. Rep. Mater. Sci. 1990;20:299–338.
[35] Tal-Gutelmacher E, Eliezer D, Abramov E. Thermal desorption spectroscopy (TDS)—application in quantitative study of hydrogen evolution and trapping in crystalline and non-crystalline materials. Mater Sci Eng, A 2007;445–446:625–31.
[36] Martin M, Gommel C, Bokhart C, Fromm E. Absorption and desorption kinetics of hydrogen storage alloys. J Alloys Compd 1996;238:193–201.
[37] Sandim HRZ, Morante BV, Suzuki PA. Kinetics of thermal decomposition of titanium hydride powder using in situ high-temperature X-ray diffraction (HTXRD). Mater Res 2005;8:293–7.
[38] Von Zeppelin F, Hirscher M, Stanzick H, Banhart J. Desorption of hydrogen from blowing agents used for foaming metals. Compos Sci Technol 2003;63:2293–300.
[39] Kovalev DY, Prokudina VK, Ratnikov VI, Ponomarev VI. Thermal decomposition of TiH_2: a TRXRD study. Int J Self-Propag High-Temp Synth 2010;19:253–7.
[40] Syrtanov M, Garanin G, Kashkarov E, Pushilina N, Kudiiarov V, Murashkina T. Laboratory X-ray diffraction complex for in situ investigations of structural phase evolution of materials under gaseous atmosphere. Metals 2020;10. article 447.
[41] Zhou Y-L, Zheng L-R, Chu S-Q, Wu M, An P-F, Zhang J, Hu T-D. In-situ EXAFS study on the thermal decomposition of TiH_2. Chin Phys C 2014;38. article 038001.
[42] Lehmhus D, Rausch G. Tailoring titanium hydride decomposition kinetics by annealing in various atmospheres. Adv Eng Mater 2004;6:313–30.
[43] Liu H, He P, Feng JC, Cao J. Kinetic study on nonisothermal dehydrogenation of TiH_2 powders. Int J Hydrogen Energy 2009;34:3018–25.
[44] Bhosle V, Baburaj EG, Miranova M, Salama K. Dehydrogenation of TiH_2. Mater Eng A 2003;356:190–9.
[45] Jiménez C, Garcia-Moreno F, Pfretzschner B, Klaus M, Wollgarten M, Zizak I, Schumacher G, Tovar M, Banhart J. Decomposition of TiH_2 studied in situ by synchrotron X-ray and neutron diffraction. Acta Mater 2011;59:6318–30.
[46] Rasooli A, Boutorabi MA, Divandari M, Azarniya A. Effect of high heating rate on thermal decomposition behaviour of titanium hydride (TiH_2) powder in air. Bull Mater Sci 2013;36:301–9.
[47] Ben David R, Finkelstein Y, Nativ-Roth E, Danon A, Cohen D, Rabkin E. The role of surface coarsening and sintering during thermal decomposition of titanium hydride. Int J Hydrogen Energy 2019;44:6045–54.
[48] Jiménez C, Garcia-Moreno F, Rack A, Tucoulou R, Klaus M, Pfretzschner B, Rack T, Cloetens P, Banhart J. Partial decomposition of TiH_2 studied in situ by energy-dispersive diffraction and ex situ by diffraction microtomography of hard X-ray synchrotron radiation. Scripta Mater 2012;66:757–60.
[49] Takasaki A, Furuya Y, Ojima K, Taneda Y. Hydride dissociation and hydrogen evolution behavior of electrochemically charged pure titanium. J Alloys Compd 1995;224:269–73.
[50] Pushilina N, Panin A, Syrtanov M, Kashkarov E, Kudiiarov V, Perevalova O, Laptev R, Lider A, Koptyug A. Hydrogen-induced phase transformation and microstructure evolution for Ti–6Al–4V parts produced by electron beam melting. Metals 2018;8. article 301.
[51] Laptev R, Kudiiarov V, Pushilina N. Hydrogen influence on defect structure and mechanical properties of EBM Ti-6Al-4V. Mater Today: SAVE Proc 2019;19:2084.
[52] Pushilina NS, Kudiiarov VN, Syrtanov MS, Kashkarov EB. Effect of the beam current during the electron-beam melting of titanium alloy Ti–6Al–4V on the structural features and phase transitions in gas-phase hydrogenation. J. Surf. Invest. X-Ray, Synchrotron Neutron Tech. 2019;13:429–33.
[53] Silverstein R, Eliezer D. Hydrogen trapping in 3D-printed (additive manufactured) Ti-6Al-4V. Mater Char 2018;144:297–304.
[54] Metalnikov P, Eliezer D, Ben-Hamu G, Tal-Gutelmacher E, Gelbstein Y, Munteanu C. Hydrogen embrittlement of electron beam melted Ti–6Al–4V. Int. J. Mater. Res. Technol. 2020;9:16126–34.
[55] Eliaz N, Eliezer D, Olson DL. Hydrogen-assisted processing of materials. Mater Sci Eng, A 2000;289:41–53.
[56] Eliezer D, Eliaz N, Senkov ON, Froes FH. Positive effects of hydrogen in metals. Mater Sci Eng, A 2000;280:220–4.
[57] Eliaz N, Eliezer D, Abramov E, Zander D, Köster U. Hydrogen evolution from Zr-based amorphous and quasicrystalline alloys. J Alloys Compd 2000;305:272–81.
[58] Hruška P, Čížek J, Knapp J, Lukáč F, Melikhova O, Mašková S, Havela L, Drahokoupil J. Characterization of defects in titanium created by hydrogen charging. Int J Hydrogen Energy 2017;42:22557–63.
[59] Kossoy E, Khoptiar Y, Cytermann C, Shemesh G, Katz H, Sheinkopf H, Cohen I, Eliaz N. The use of SIMS in quality control and failure analysis of electrodeposited items inspected for hydrogen effects. Corrosion Sci 2008;50:1481–91.
[60] Ifergane S, Ben David R, Sabatani E, Carmeli B, Beeri O, Eliaz N. Hydrogen diffusivity and trapping in Custom 465® stainless steel. J Electrochem Soc 2018;165:C107–15.
[61] Zhu T, Li M. Lattice variations of Ti-6Al-4V alloy with hydrogen content. Mater Char 2011;62:724–9.
[62] Zhang Y, Zhang SQ. Hydrogenation characteristics of Ti-6Al-4V cast alloy and its microstructural modification by hydrogen treatment. Int J Hydrogen Energy 1997;22:161–8.
[63] Bonaccorsi L, Calabrese L, Pintaudi A, Proverbio E, Aliotta F, Ponterio R, Scherillo A, Tresoldi D. Reversible hydrogen absorption in a Ti-6Al-4V alloy produced by mechanical alloying. Int J Hydrogen Energy 2014;39:15540–8.
[64] Rautray TR, Narayanan R, Kim K-H. Ion implantation of titanium based biomaterials. Prog Mater Sci 2011;56:1137–77.
[65] Vogel SC, Takajo S, Kumar MA, Caspi EN, Pesach A, Tiferet E, et al. Ambient and high-temperature bulk characterization of additively manufactured Ti–6Al–4V using neutron diffraction. JOM (Journal of Metals) 2018;70:1714–22.